The Influence of the Simultaneous Addition of Fe^{2+} and Fe^{3+} on Changes in the Structural, Optical, and Electronic Properties of TiO_2 Powder

Candra Purnawan[1,2], Endang Tri Wahyuni[1,*], Indriana Kartini[1] and Suherman[1]

[1]Department of Chemistry, Faculty of Mathematics and Natural Sciences, Gadjah Mada University, Yogyakarta 55281, Indonesia

[2]Department of Chemistry, Faculty of Mathematics and Natural Sciences, Sebelas Maret University, Jawa Tengah 57126, Indonesia

([*]Corresponding author's e-mail: endang_triw@ugm.ac.id)

Abstract

Modification of TiO_2 powder to form TiO_2-Fe/Fe_2O_3 composites with simultaneous incorporation of Fe^{2+} and Fe^{3+} ions via a simple approach has been conducted. The characterization of photocatalyst composites has been carried out using FTIR, Raman, XRD, SAA, TEM, DRS, XPS, and VSM. The simultaneous incorporation of Fe^{2+} and Fe^{3+} ions has modified the structural, optical, and magnetic properties of TiO_2 powder. Systematic variation of Fe^{2+}: Fe^{3+} compositions (mole/mole) revealed that Fe^{3+} had a stronger impact than Fe^{2+}. At low Fe^{3+} and Fe_2O_3 composition, interfacial interaction and heterojunction formation dominated, whereas higher levels promoted substitutional doping. At low Fe^{3+} composition (Fe^{2+}: Fe^{3+} = 1:0.3 - 1:1), crystallite size increased (29.95 - 34.65 nm) but crystallinity decreased (62.34% - 57.99%), surface area increased (25.90 - 29.71 m^2/g) but pore size decreased (0.097 - 0.085 cc/g), the bandgap narrowed (3.14 - 2.98 eV), and maghemite formation and magnetic moment decreased (36.83 - 17.66 emu/g). Whereas at Fe^{3+} higher ratio (Fe^{2+}: Fe^{3+} = 1:1 - 1:3), the bandgap significantly narrowed (2.98 - 2.80 eV), crystallite size (34.65 - 27.30 nm) and crystallinity (57.99% - 49.27%) decreased, surface area (29.09 - 43.49 m^2/g) and pore size (0.085 - 0.139 cc/g) increased, and hematite formation increased and magnetic moment decreased (17.66 - 14.86 emu/g). Furthermore, increasing the proportion of Fe_2O_3 in TiO_2 powder (TiO_2: Fe_2O_3) has enlarged the surface area and pore size, narrowed the bandgap, decreased the crystallite sizes and crystallinity, and improved magnetic properties. Photocatalytic evaluation under visible light showed that increasing Fe^{3+} and Fe_2O_3 enhanced both Methyl Violet (MV) degradation up to 84.54% and Cr(VI) reduction up to 36.55%, with stronger MV degradation indicating that Fe^{3+} mainly serves as an electron trap.

Keywords: TiO_2 powder, Fe^{2+}: Fe^{3+} ratio, TiO_2: Fe_2O_3 ratio, Simultaneous, Structural, Optical, Electronic, Properties

Introduction

Titanium dioxide (TiO_2) is a widely used semiconductor photocatalyst due to its high photocatalytic efficiency, chemical stability, non-toxicity, and low cost. However, its wide bandgap (3.2 eV) limits visible-light activity, and its recovery after use remains inefficient [1,2]. To overcome the limitations, modifications such as Fe doping have been extensively explored. Iron is a common transition metal that can reduce bandgap and provide magnetic properties. Fe^{3+} ion can substitute Ti^{4+} due to their similar ionic radii, thereby narrowing the bandgap and

imparting magnetic properties. Ferric ion (Fe^{3+}) can function as dopants because both Fe^{3+} (0.64 Å) and Ti^{4+} (0.68 Å) ions have similar sizes [1]. In oxide form, Fe can also function as a photocatalyst, magnetic agent, heterojunction, or adsorbent. However, most reported approaches apply doping and magnetization separately, often through sol-gel synthesis using TiO_2 precursors, which is costly, complex, time-consuming, difficult reaction control, and less feasible for large-scale applications [3,4].

Recent studies have also employed TiO_2 powder via hydrothermal or co-precipitation methods to simplify synthesis, though the high stability of anatase limits ion incorporation because TiO_2 powder is a crystal with excellent chemical and physical stability. Shymanovska *et al*. [2] have conducted Fe^{3+} ion doping on TiO_2 Anatase and Rutile powders. The results have demonstrated that the adsorption of Fe^{3+} ions on the surface of Anatase is twice as efficacious as that of Rutile. The adsorption of Fe^{3+} ions on the TiO_2 surface causes changes in the crystal lattice, bandgap, and acidity. However, the photocatalytic activity of Safranin T degradation using Fe^{3+} doped TiO_2 is lower than TiO_2 without doping. Meanwhile, Afonso *et al*. [5] found that Fe^{3+}-doped TiO_2 photocatalysts lacked magnetic characteristics and had worse RhB photodegradation efficiency (<70%) than undoped TiO_2 (74%) under visible light irradiation. Thus, further research is needed to simultaneously enhance photocatalytic activity under visible light and improve catalyst separability through magnetization.

In this study, TiO_2 powder will be modified with simultaneous incorporation of Fe^{2+} and Fe^{3+} ions via a simple approach to form TiO_2-Fe/Fe_2O_3 composites. The simultaneous addition of Fe^{2+} and Fe^{3+} is expected to improve electronic and optical properties, visible-light photocatalytic activity, and magnetic separability by doping (TiO_2-Fe) and heterojunction (TiO_2/Fe_2O_3) mechanism. The incorporation of Fe^{2+} and Fe^{3+} ions to TiO_2 powder will provide a different mechanism and alter its characteristics in contrast to utilizing TiO_2 precursors, so further research is needed. The success of this study offers a new approach to TiO_2 powder modification, simplifying the process and making its application in wastewater treatment more cost-effective and practical. Variations in Fe^{2+}/Fe^{3+} and Fe_2O_3/TiO_2 ratios (mole/mole) play a crucial role in modifying the properties and activity of TiO_2 powder. The composition will induce changes in electron density, interactions, lattice distortion and deformation, structure regularity, crystallinity and crystallite size, bandgap, electron binding energy, surface area, and magnetic behavior, thereby changing structure, electronic, and optical properties so that finally change photocatalytic performance. To determine the effects, the photocatalyst composite will be characterized using FTIR, Raman, XRD, SAA, TEM, DRS, XPS, and VSM.

Materials and methods
Materials

Titanium (IV) Oxide Anatase >99% (Sigma-Aldrich), Iron(III) Chloride hexahydrate (Merck), Iron(II) Chloride Tetrahydrate (Merck), Sodium Hydroxide (Merck), Isopropanol (Merck), Potassium dichromate (Merck), Methyl violet (Loba Chemie PVT, LTD), Demineralized Aqua with TDS < 1.3 µS/cm (Brataco), Acetone (Merck), Nitric Acid (Merck), Diphenylcarbazide (Merck), Chloroform (Merck), Phosphoric Acid (Merck).

Synthesis of TiO_2-Fe/Fe_2O_3 for modification of TiO_2 powder

Composite TiO_2-Fe/Fe_2O_3 had been synthesized using TiO_2 Anatase powder, $FeCl_3.6H_2O$ and $FeCl_2.4H_2O$. A quantity $FeCl_3.6H_2O$ and $FeCl_2.4H_2O$ with theoretical mole ratio of Fe^{2+}: Fe^{3+} = 1:0.3; 1:0.5; 1:1; 1:2; 1:3 (mole/mole) were dissolved in 25 mL of distilled water and added with a number of TiO_2 Anatase powder in 25 mL of isopropanol with theoretical mole ratio of TiO_2: Fe_2O_3 = 1: $\frac{1}{20}$(TF$_{0.05}$); 1: $\frac{1}{15}$ (TF$_{0.07}$); 1: $\frac{1}{10}$ (TF$_{0.1}$); 1: $\frac{1}{5}$ (TF$_{0.2}$) dan 1:1 (FT$_{1.0}$) (mole/mole). Then, 50 mL of distilled water was added to the mixture and stirred for 1 h (400 rpm). Next, add drop by drop NaOH 10 M until the pH = 12while stirring continuously for 1 h (700 rpm). Then the mixture was heated at 90 °C for 1 h while stirring continuously. The black or gray composite formed was dried overnight at 60 °C (24 h). After grinding into powder, the granules were calcined in a muffle furnace at 400 °C for 2 h. The synthesized composite was rinsed with demineralized water until it reached a neutral pH and dried again overnight in a 60 °C oven (12 h) and then characterized using Fourier Transform InfraRed (FTIR) Spectroscopy, Raman Spectroscopy, Diffused Reflectance Spectroscopy (DRS), X-Ray Diffraction Spectroscopy (XRD), Vibrating Sample Magnetometer (VSM), Transmission Electron Microscope (TEM), Surface Area Analyzer (SAA), and X-ray photoelectron spectroscopy (XPS).

Results and discussion

The influence of Fe^{2+}: Fe^{3+} composition (mole/mole)

In this section, TiO_2-Fe/Fe_2O_3 photocatalyst have been synthezised with a constan mole ratio of TiO_2: Fe_2O_3 = 1:1/5 ($TF_{0.2}$). Meanwhile, the variation of Fe^{2+}: Fe^{3+} was carried out at mole ratio Fe^{2+}: Fe^{3+} = 1:0.3, 1:0.5, 1:1, 1:2 and 1:3 (mole/mole).

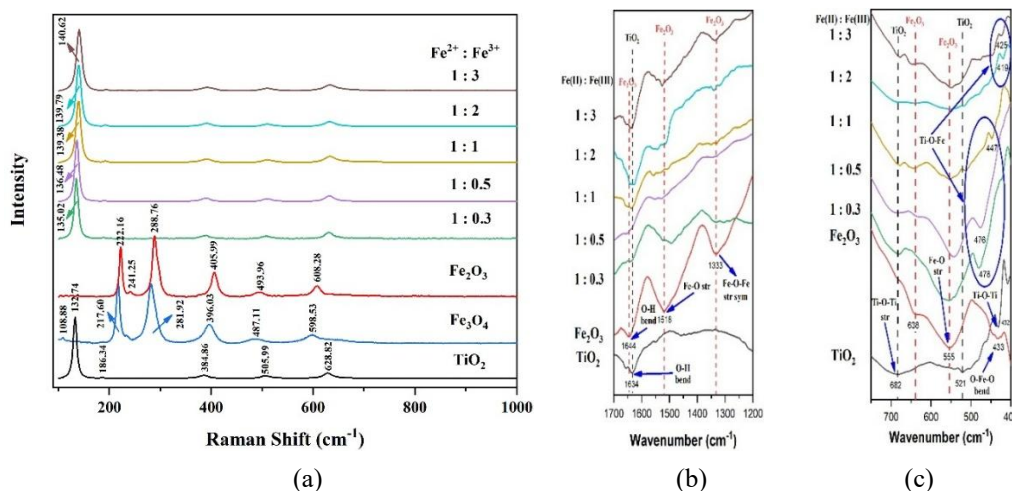*Raman and FTIR Analysis.* The simultaneous addition of Fe^{2+} and Fe^{3+} with different composition into TiO$_2$ powder influences Raman inelastic scattering and vibrational energy, as shown in **Figure 1**. Based on Raman spectra (**Figure 1(a)**), the characteristic TiO_2 peaks include E_g at 132.74 cm^{-1} (O-Ti-O symmetric stretching), B_{1g} at 384.86 cm^{-1} (O-Ti-O symmetric bending), B_{1g} + A_{1g} at 505.99 cm^{-1} (symmetric/asymmetric bending), and E_{3g} at 628.82 cm^{-1} (Ti-O stretching) [6,7]. The asymmetric O-Ti-O vibration is associated with Ti^{3+} or oxygen vacancy defects [8].

Figure 1 (a) Raman, and (b) - (c) FTIR Spectra of TiO_2, Iron Oxide, and composites in the variation of composition Fe^{2+}: Fe^{3+} (mole/mole).

Figure 1(a) also showed that calcination induces the transformation of Fe_3O_4 (blue) to Fe_2O_3 (red), as indicated by the disappearance of Magnetite peaks at 108.88 and 647.06 cm^{-1} and the emergence of a new peak at 241.25 cm^{-1} [9]. The shifts at 217.60 and 281.92 cm^{-1} confirm the oxidation of Fe^{2+} to Fe^{3+} during the process [10]. The increased intensity ratio of the 281.92 cm^{-1} peak to the 217.60 cm^{-1} peak further supports the increasing of Fe^{3+} after calcination. Raman analysis further revealed that increasing Fe^{3+} content shifts the main E_g peak from 132.74 to 140.62 cm^{-1}, indicating enhanced lattice distortion and doping process. The peak shift and broadening at higher dopant levels confirm lattice deformation and defect formation due to Fe^{3+} substitution for Ti^{4+} in the TiO_2 lattice [6,11]. When Fe^{3+} substitutes Ti^{4+} ions, oxygen vacancies and lattice distortions are generated to maintain local charge neutrality, leading to Raman peak shifts and broadening. The resulting oxygen deficiency and structural distortion locally shorten Ti-O bonds, while the overall lattice d-spacing decreases, causing the Raman peaks to shift toward higher wavenumbers. Compared to Fe^{2+}, Fe^{3+} induces stronger distortion, consistent with the increased intensity of hydroxyl groups at 1634 cm^{-1} and Ti-O-Fe bending vibrations, as shown in **Figures 1(b)** and **1(c)**. A new peak appears at 478 - 419 cm^{-1}, assigned to Ti-O-Fe bending vibrations, confirming Fe^{3+} incorporation into the TiO_2 lattice as substitutional dopants replacing Ti^{4+}. The red shift evidences substitutional doping, which is also characterized by Fe-O vibrations shifting to lower wavenumbers [12].

XRD Analysis. Ratio of Fe^{2+}: Fe^{3+} (mole/mole) have affected the diffractogram pattern and crystal composition of composite as shown in **Figure 2**. The diffractogram pattern of Anatase TiO_2, Maghemite (γ-Fe_2O_3), Hematite (α-Fe_2O_3) are consistent with the diffractogram of ICSD standard No. 9852, ICSD No. 172905, and ICSD No. 164008, respectively.

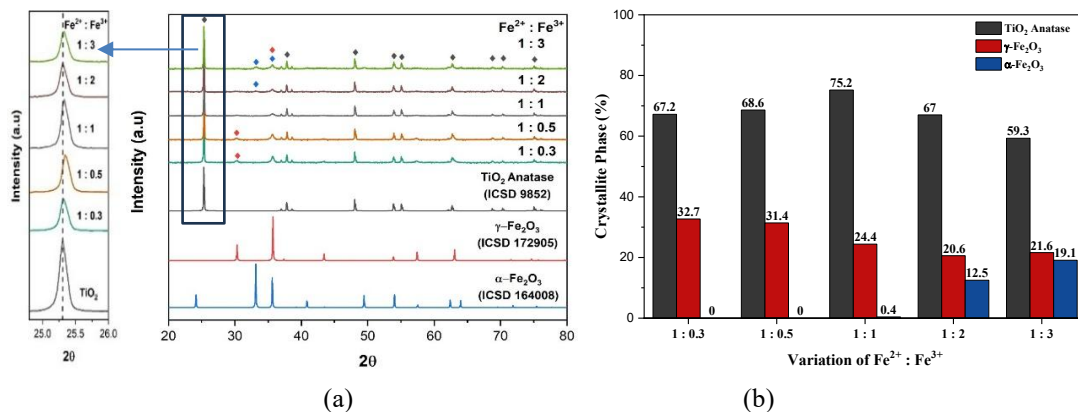(a)   (b)

Figure 2 (a) XRD diffractogram, and (b) Crystallite composition (%) of the composite with Fe^{2+}: Fe^{3+} composition (mole/mole).

Figure 2(a) showed the excessive Fe^{2+} or Fe^{3+} content reduced the intensity of TiO_2 peaks at $2\theta = 25.3°$, $37.8°$, $48.0°$ and $62.72°$, compared with the Fe^{2+}: $Fe^{3+} = 1:1$ composite, indicating a decline in TiO_2 crystallinity and crystallite composition due to Fe ion distortion and deformation. The phenomenon is confirmed with crystal composition using HighScore Plus software as shown in **Figure 2(b)**. **Figure 2(b)** illustrated the effect of Fe^{2+}: Fe^{3+} composition on TiO_2 crystallite structure and the formation of Maghemit and Hematit. Fe^{3+} more effectively reduces TiO_2 crystallite composition than Fe^{2+}, induces stronger lattice distortion and defects, and then facilitates substitutional doping. The presence of substitutional doping causes distortion and structural defects [13]. A higher Fe^{2+} ratio favors

Maghemit formation, whereas excess Fe^{3+} decreases Maghemit and promotes Hematit through $Fe(OH)_3$ transformation. A higher Fe^{3+} composition promotes greater $Fe(OH)_3$ formation and its subsequent transformation into hematite (α-Fe_2O_3). Thus, at high Fe^{3+} levels, hematite primarily originates from both maghemite and $Fe(OH)_3$ transformation, whereas at low Fe^{3+} levels, it mainly results from maghemite transformation.

The presence of Fe^{2+} and Fe^{3+} ions can also affect the crystallinity index and crystallite size of photocatalyst, as seen in **Figure 3**. This crystallinity was calculated based on Wibowo *et al*. [14], and crystal size was obtained based on the Scherrer equation [15].
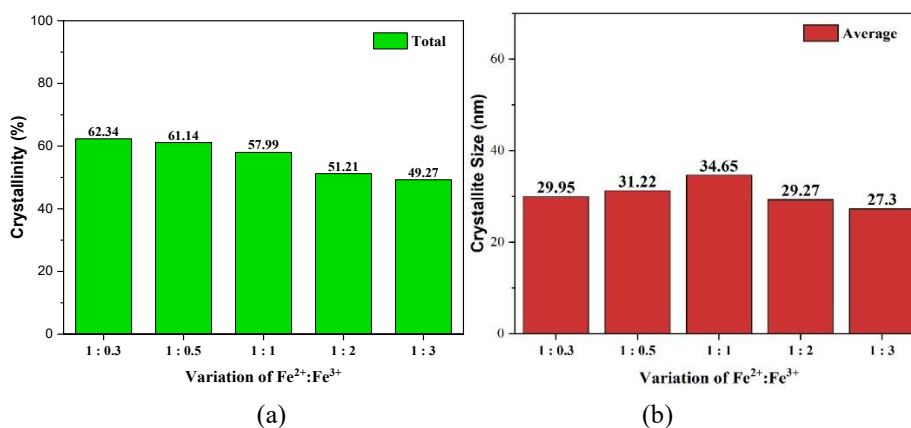

(a)   (b)

Figure 3 (a) Crystallinity index, (b) Crystal size of photocatalyst composite.

Figure 3(a) indicated that Fe^{3+} more effectively suppresses TiO_2 crystallinity than Fe^{2+} due to its smaller ionic radius and higher charge, which enhance lattice distortion and disorder [5,16]. As shown in **Figure 3(b)**,

at low Fe^{3+} levels (Fe^{2+}: $Fe^{3+} = 1:0.3$ - $1:1$) promote interfacial interactions between TiO_2 and Fe_2O_3 so that enlarge particle growth and crystallite size [1,17]. The interfacial interactions such as sintering, coupling, or

aggregation facilitate heterojunction formation. Whereas, at higher Fe^{3+} compositions (Fe^{2+}: Fe^{3+} = 1:1 - 1:3), it induces severe distortion and defects, reducing both crystallinity and crystallite size, and then facilitates Fe ion doping. Loan *et al*. [11] stated that the greater the Fe^{3+} doping into TiO_2, the smaller the crystallite size. The greater the Fe^{3+} doping, the greater the distortion and defects so that the deformation becomes greater and the crystallite size becomes smaller.

Surface Area Analysis (SAA). Mole ratio of Fe^{2+}: Fe^{3+} have also affected the surface area of composite as shown in **Figure 4**. **Figure 4(a)** displayed a type IV

adsorption isotherm typical of mesoporous materials (2 - 50 nm), with an H3 (slit-shaped pores or plate-like aggregates) or H4 (wedge-shaped pores) hysteresis loop associated with slit or wedge-shaped pores formed by particle irregularities, non-uniform pore structures, incomplete or asymmetric openings, non-linear channels, and broad pore size distribution [18,19]. As shown in **Figure 4(b)**, increasing Fe^{3+} composition enhances surface area and pore volume more effectively than Fe^{2+} due to stronger lattice distortion, as supported by increased hydroxyl groups **(Figure 1(b))**, and decreased crystallinity **(Figure 3(a))**.
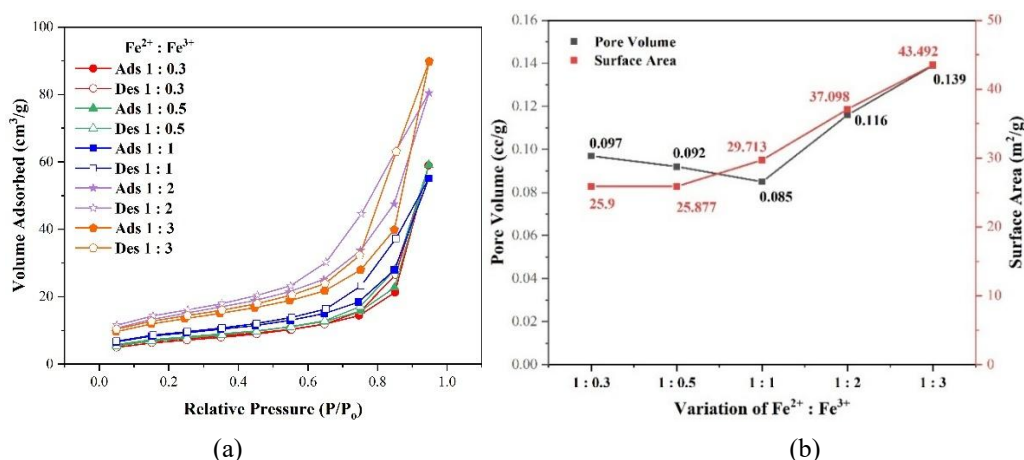

(a)   (b)

Figure 4 (a) Hysteresis loop Isotherm, (b) Pore volume and surface area of composite with Fe^{2+}: Fe^{3+} composition (mole:mole).

At low Fe^{3+} composition (Fe^{2+}: Fe^{3+} = 1:0.3 - 1:1), distortion is insufficient to significantly deform the TiO_2 lattice, and surface area increases mainly through interfacial interactions, accompanied by reduced pore volume. In contrast, higher Fe^{3+} composition (Fe^{2+}: Fe^{3+} = 1:1 - 1:3) induces substitutional doping, oxygen vacancies, and severe lattice deformation, which open and enlarge TiO_2 pores, leading to increased internal pore volume, irregularities, and surface area. Surface area is mainly interpreted as internal area (intraparticle porosity) with additional contribution from surface irregularities. Internal porosity contributes more significantly to surface area than particle size effects [13,20].

Bandgap analysis. The change in Fe^{2+}: Fe^{3+} composition causes a variation in the interaction and distortion strength of the TiO_2 crystal and alters the formation of iron oxide, thereby affecting the doping strength and interfacial interactions. Then, in turn, the composition will influence the bandgap of the photocatalyst composite, as shown in **Figure 5**. The optical energy bandgap of composite has been estimated using Tauc's Plot equation [$(\alpha h\upsilon)^{1/n} = K (h\upsilon - E_g)$] with plotting $(\alpha h\upsilon)^2$ vs $h\upsilon$. The linier part of the curves is extrapolated such that the intercept on the energy axis $(\alpha h\upsilon)^2 = 0$ gives the energy bandgap.
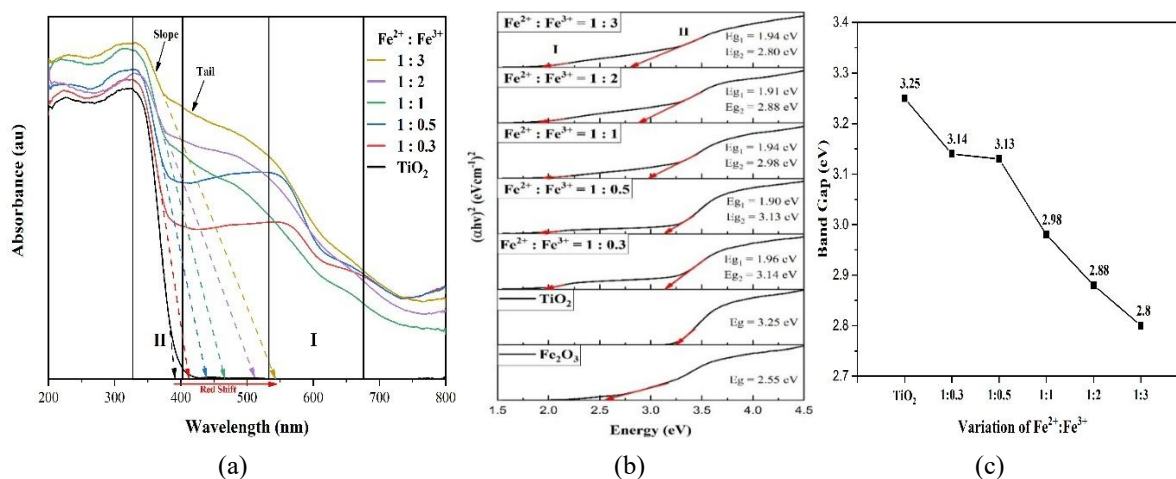
Figure 5 (a) DRS spectra, (b) tauc plots, and (c) band gap of composites with Fe^{2+}: Fe^{3+} composition (mole:mole).

Figure 5 showed that increasing Fe^{3+} composition reduces the composite bandgap from 3.25 to 2.80 eV. The decreasing is attributed to 2 main mechanisms: Heterojunction formation between TiO_2 and Fe_2O_3, and Fe^{3+} doping. At lower Fe^{3+} content (Fe^{2+}: Fe^{3+} = 1:0.3 - 1:1), bandgap narrowing is dominated by heterojunction formation, driven by interfacial interactions (sintering, coupling, aggregation) that modify the electronic structure without significantly altering TiO_2 intrinsic absorption slope and bandgap (Area II). Interfacial interaction does not directly change the intrinsic bandgap of TiO_2 but occurs through heterojunction formation [21]. The energy band gap of Fe_2O_3/TiO_2 nanocomposites decreased as the Fe_2O_3 loading increased which can be attributed to the formation of heterojunction structure, and the formation of a new molecular orbital that results in reduced bandgap accordingly [3]. The formation of a heterojunction between TiO_2 and Fe_2O_3 involves the combination of two semiconductors with different band gaps. Since TiO_2 possesses a higher Fermi energy and lower work function than Fe_2O_3, electron transfer occurs from TiO_2 to Fe_2O_3 to equilibrate their Fermi levels.

At higher Fe^{3+} content (1:1 - 1:3), distorsion and doping becomes dominant, where Fe^{3+} substitutes Ti^{4+}, enhances orbital overlap (Ti 3d-Fe 3d), and introduces mid-gap states, Ti^{3+}, and oxygen vacancies [22]. Fe^{3+} ions substitute Ti^{4+} ions in TiO_2 crystal and cause a change in the band gap by forming their mid gap energy levels in the respective samples along with the formation of Ti^{3+} and oxygen vacancies [22]. The defects lead to a red-shift of the absorption edge, broadening of the absorption tail and narrowing the bandgap, consistent with previous reports [2,23]. The decrease in bandgap due to doping has also been supported by the decrease in crystal size (**Figure 3(b)**) which is not accompanied by an increase in bandgap (**Figure 5(b)**) from the composition Fe^{2+}: Fe^{3+} = 1:1 - 1:3. Ideally, the decrease in crystallite size at nanoscale should increase the bandgap but the presence of Fe^{3+} doping has caused a decrease in the composite bandgap [24,25]. The decrease in bandgap due to doping confirmed the Raman analysis (**Figure 1**).

XPS Analysis. XPS spectra of TiO_2 and composites with Fe^{2+}: Fe^{3+} composition as seen in **Figure 6**. The composite used in this study was the $TF_{0.2}$ composite with the composition of Fe^{2+}: Fe^{3+} = 1:0.3, 1:1 and 1:3 (mole/mole).

(a)   (b)

(c)   (d)

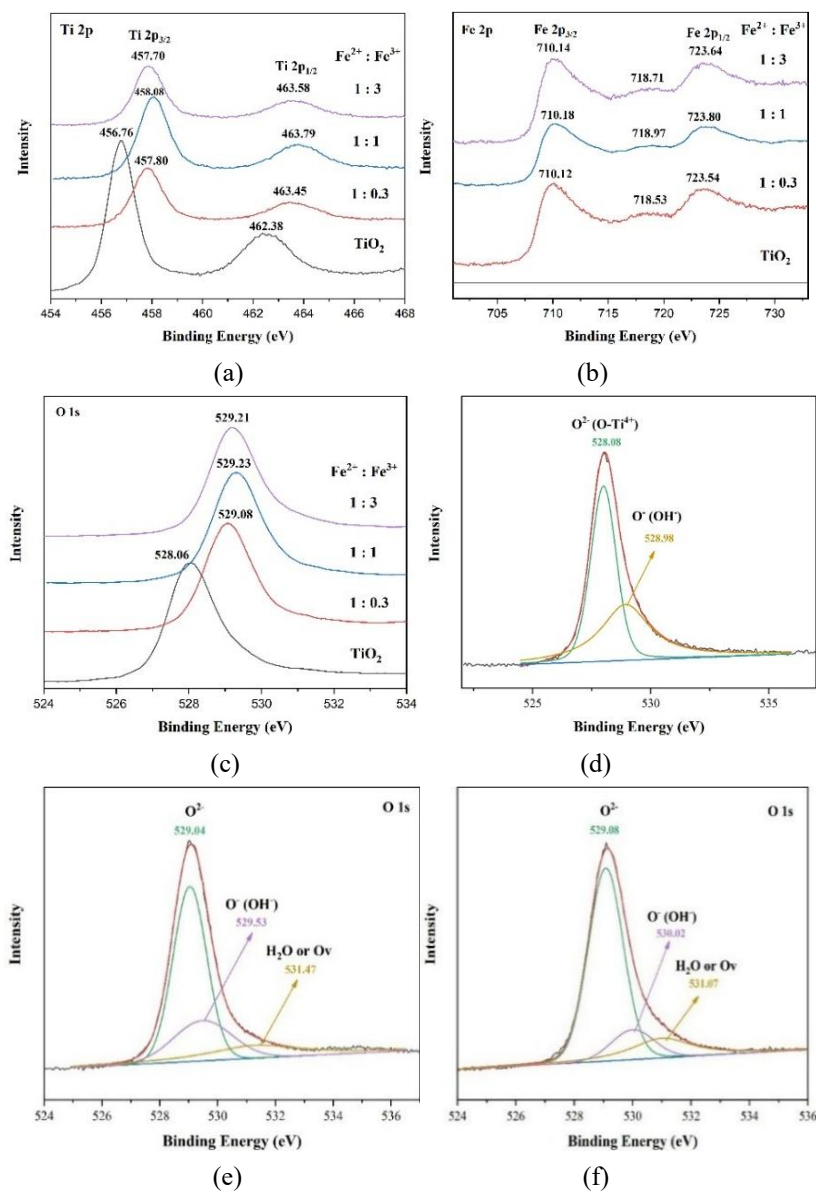(e)   (f)

Figure 6 XPS spectra of composites (a) high resolution spectra (HRS) of Ti2p peak, (b) high resolution spectra (HRS) of Fe 2p peak (c) high resolution spectra (HRS) of O 1s peak, (d) deconvolution spectra O1s of TiO_2, (e) deconvolution spectra O1s of Fe^{2+}: Fe^{3+} = 1:0.3, (f) deconvolution spectra O1s of Fe^{2+}: Fe^{3+} = 1:3.

Figure 6(a) showed Ti 2p peaks at 456.8 eV ($2p_{3/2}$) and 462.4 eV ($2p_{1/2}$), with a spin spillting of 5.65 - 5.88 eV, confirming Ti^{4+}. Incorporation of Fe ions causes binding energy shifts in both Ti 2p peaks, indicating Fe-O-Ti bond formation. At lower Fe^{3+} content (Fe^{2+}: Fe^{3+} = 1:0.3 - 1:1), a positive shift of Ti 2p suggests heterojunction formation, driven by electron transfer from TiO_2 (higher Fermi level) to Fe_2O_3 (lower Fermi level), which reduces TiO_2 electron density and increases binding energy. At higher Fe^{3+} content (Fe^{2+}: Fe^{3+} = 1:1 - 1:3), a negative Ti 2p shift occurs (~0.1 - 0.5 eV) due to substitutional doping of Ti^{4+} by Fe^{3+}, which generates oxygen vacancies and promotes Ti^{3+}

formation as a charge compensation mechanism, then subsequently increasing the electron density and reducing the binding energy of Ti 2p [16,26]. Consistently, binding energy of O 1s spectra (**Figure 6(c)**) also exhibits positive shifts (528.06 → 529.23 eV) with increasing Fe^{3+}, attributed to charge redistribution from Ti^{4+} substitution by Fe^{3+}, consistent with lattice distortion and oxygen vacancy formation [16,27]. Based on **Figures 6(d)** - **6(f)**, the deconvoluted O 1s spectra showed a new peak at 531.17 eV, absent in pure TiO_2 (**Figure 6(d)**), which indicated the presence of oxygen vacancies, with intensity increasing as Fe^{3+} content rises. The results demonstrated that higher Fe^{3+} content

enhances oxygen vacancy formation and Fe-O-Ti bonding, mainly through substitutional doping [26]. So that in this case, not only the interfacial interaction and heterojunction occurred but also the doping increased with increasing Fe^{3+} composition.

VSM Analysis. Vibrating Sample Magnetometry (VSM) analysis was performed to investigate the alteration of magnetic properties in TiO_2 powders upon the simultaneous incorporation of Fe^{2+} and Fe^{3+} ions, as shown in **Figure 7** and **Table 1**.
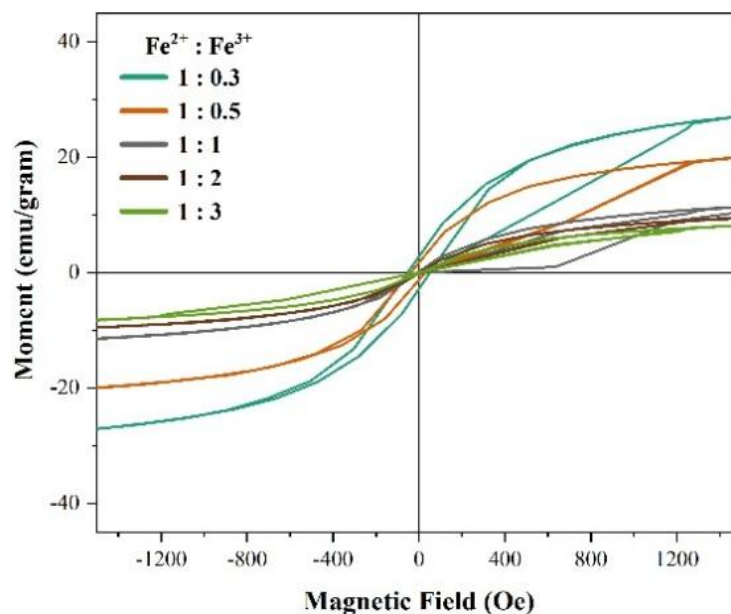

Figure 7 (a) VSM Loop hysteresis of composite with variation of Fe^{2+}: Fe^{3+} (mole/mole).

Table 1 Saturation Magnetization (Ms), Remanence Magnetisation (Mr), and Coercivity (Oe) composite.

Composition of Fe^{2+}: Fe^{3+}	Ms (emu/gram)	Mr (emu/gram)	Hc (Oe)
TiO_2 (control)	0.01	0	0
1:0.3	36.83	2.80	51.99
1:0.5	26.25	1.54	33.86
1:1	17.66	0	0
1:2	15.92	0	0
1:3	14.86	0	0

Figure 7 and **Table 1** indicated that the composite exhibits soft magnetic behavior, characterized by a narrow hysteresis loop, low remanence (Mr), and low coercivity (Hc < 1kA/m). At low Fe^{3+} composition (0.3:0.5 mole), Loop hysteresis showed ferromagnetic behavior with coercivity (Hc) 51.99 and 33.86 Oe, whereas at high Fe^{3+} composition (1:2 mole) showed super-paramagnetic behavior with zero coercivity (Hc) and remanence (Mr). Increasing Fe^{3+} composition decreases the saturation magnetization (Ms) from 36.83 to 14.86 emu/g due to the higher fraction of hematite (α-Fe_2O_3), which is paramagnetic, consistent with XRD results (**Figure 2**). In hematite structure, Fe^{3+} ions occupy symmetrical octahedral sites with antiparallel spins, resulting in a nearly zero net magnetic moment. In contrast, maghemite contains Fe^{3+} ions in both octahedral and tetrahedral sites, creating cation imbalance and vacancies, which prevent complete spin cancellation, producing a measurable net magnetic moment [28].

The influence of TiO_2: Fe_2O_3 composition (mole/mole)

In this section, TiO_2-Fe/Fe_2O_3 photocatalysts were synthesized at a fixed Fe^{2+}: Fe^{3+} ratio of 1:2 (mole/mole). The TiO_2: Fe_2O_3 (TF) composition was varied at molar

ratios of = 1:1/20 (TF$_{0.05}$); 1:1/15 (TF$_{0.07}$); 1:1/10 (TF$_{0.1}$); 1:1/5 (TF$_{0.2}$), and 1:1 (FT$_{1.0}$) (mole/mole).

Raman and FTIR Analysis. The concentration of Fe^{2+} and Fe^{3+}, as well as the composition of Fe$_2$O$_3$ to TiO$_2$ powder, has impacted Raman light scattering (inelastic) and vibrational energy, as shown in **Figure 8**.
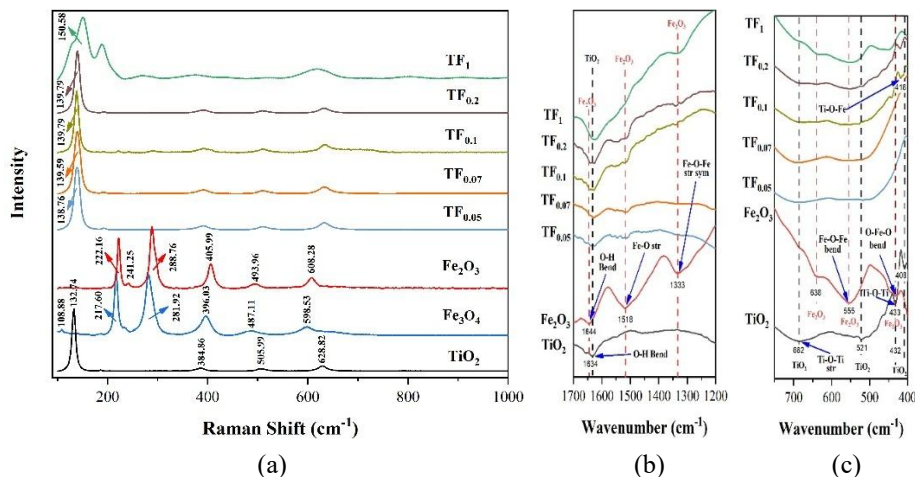

Figure 8 (a) Raman, and (b) - (c) FTIR spectra of composites with TiO$_2$: Fe$_2$O$_3$ composition.

Figure 8(a) indicated that as Fe$_2$O$_3$ composition increases, peak shifts towards higher wavenumbers occur, particularly the primary peak (E1g) from 132.74 - 150.58 cm^{-1}. The shift indicated that the higher the concentration of Fe^{2+} and Fe^{3+} with increasing Fe$_2$O$_3$ composition, the greater the polarization of the electron and the distortion of the TiO$_2$ crystal, resulting in a larger Raman shift and decreased crystallinity. A higher Fe^{3+} content extends the Eg peak toward higher wavenumbers, consistent with previous reports [6,11]. The Raman peak shift can be attributed to the lattice distortion caused by the replacement of Ti^{4+} with Fe^{3+} in the TiO$_2$ framework, which is supported by FTIR analysis (**Figures 8(b)** and **8(c)**). **Figure 8(c)** showed a new peak appears at 478 - 415 cm^{-1} at TF$_{0.1}$ - TF$_1$, assigned to Ti-O-Fe bending vibrations, confirming Fe^{3+} incorporation into the TiO$_2$ lattice as substitutional dopants replacing Ti^{4+}. Whereas at low Fe$_2$O$_3$ composition (TF$_{0.05}$ - TF$_{0.07}$), there is no peak at 478 - 419 cm^{-1}.

XRD Analysis. Alteration in the diffraction pattern of the composite with a composition of TiO$_2$:Fe$_2$O$_3$ (TF$_{0.05}$ - TF$_1$) as shown in **Figure 9**. **Figure 9** indicated that the TiO$_2$ powder is anatase, and the iron oxide is a mixture of Maghemite and Hematite with a composition of TiO$_2$:Fe$_2$O$_3$ (TF$_{0.05}$ - TF$_1$). **Figure 9(a)** revealed enhanced peak intensities of Maghemite (γ-Fe$_2$O$_3$) at 2θ = 35.71° (311) and Hematite (α-Fe$_2$O$_3$) at 2θ = 33.14° (104), indicating their increased formation with higher Fe$_2$O$_3$ content. Meanwhile, **Figure 9(a)** also showed that increasing Fe$_2$O$_3$ content (TF$_{0.2}$ → TF$_1$) induces a shift of the TiO$_2$ diffraction peak at 2θ = 25.31° (101) toward higher angles, accompanied by peak broadening and intensity reduction. The behavior confirms Fe^{3+} incorporation into the TiO$_2$ lattice, as the smaller ionic radius of Fe^{3+} (0.64 Å) compared to Ti^{4+} (0.68 Å) reduces the interplanar spacing [29]. Moreover, the decrease in peak intensity and crystallinity of TiO$_2$ is the main effect of Fe doping with increasing Fe concentration [15]. Rietveld refinement using HighScore Plus revealed a reduction in TiO$_2$ crystallite size and enhanced formation of hematite (α-Fe$_2$O$_3$) and maghemite (γ-Fe$_2$O$_3$) with increasing Fe$_2$O$_3$ composition (TF$_{0.05}$ - TF$_1$), as illustrated in **Figure 9(b)**.

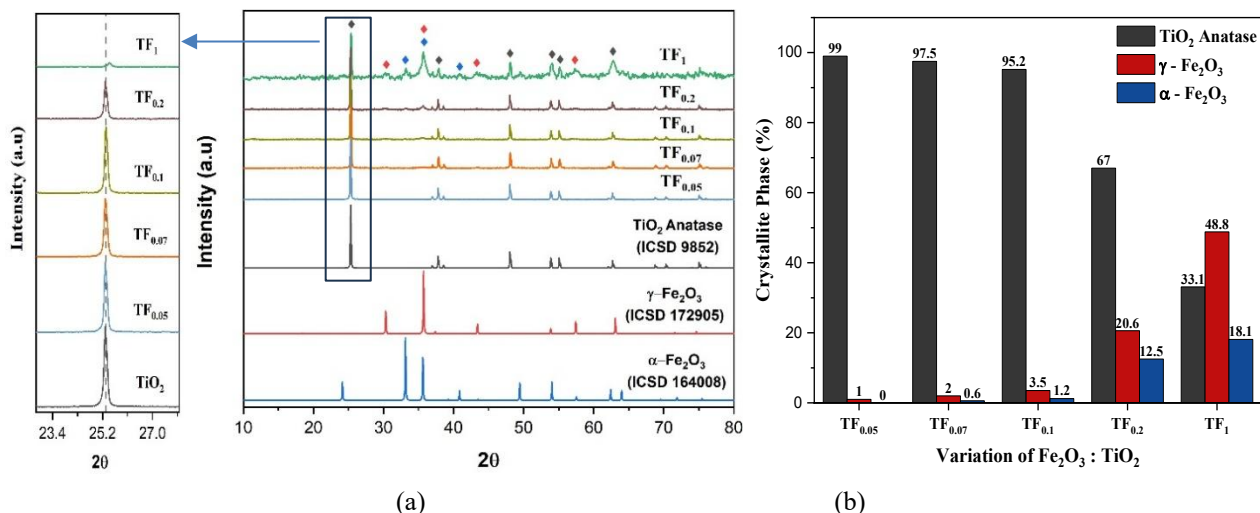(a)   (b)

Figure 9 (a) XRD diffractogram and (b) Crystallite composition (%) of composites with TiO_2: Fe_2O_3 composition.

The TiO_2: Fe_2O_3 composition also affected the crystallinity index and crystal size of photocatalyst, as seen in **Figure 10**. As shown in **Figure 10(a)**, the crystallinity index decreases progressively with higher Fe_2O_3, attributed to stronger electrostatic interactions, lattice distortion, and defects, consistent with increased hydroxyl groups (**Figure 8(b)**) [5]. The phenomenon indicated that the doping of Fe^{3+} decreased the crystallization of TiO_2 [16].
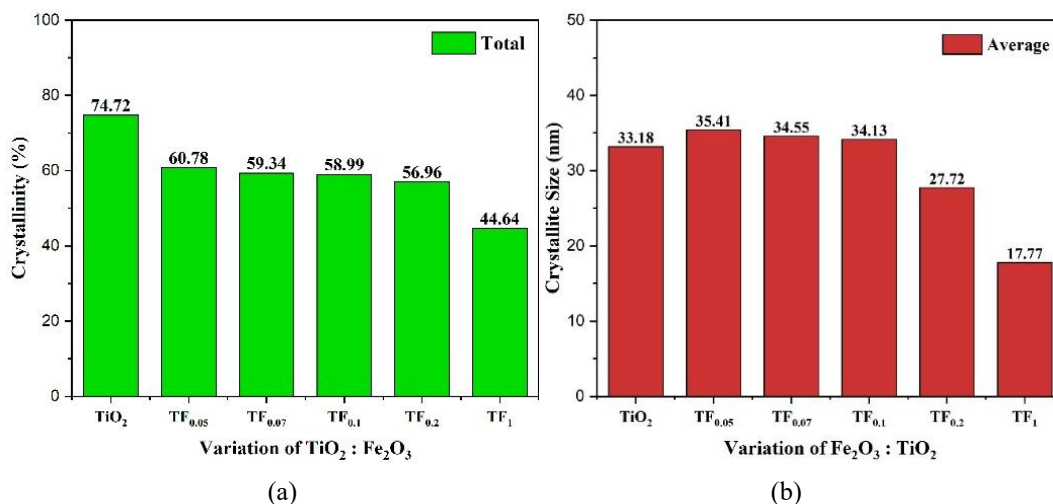

(a)   (b)

Figure 10 (a) Crystallinity index and (b) Crystal size of composite with TiO_2: Fe_2O_3 composition.

Figure 10(b) showed that at low Fe_2O_3 contents (TF$_{0.05}$ - TF$_{0.1}$), crystallite size increases compared to pure TiO_2, suggesting interfacial interactions (sintering, coupling, aggregation) that promote heterojunction formation. However, at higher Fe_2O_3 levels (TF$_{0.2}$ - TF$_1$), excessive doping and distortion dominate, leading to greater deformation and reduced crystallite size. Loan *et al*. [11] stated that the greater the Fe^{3+} doping into TiO_2, the smaller the crystallite size. These results confirm that Fe^{3+} doping both suppresses TiO_2 crystallization and induces size reduction, whereas interfacial effects at low Fe_2O_3 promote temporary crystallite growth.

SAA Anlaysis. SAA analysis was performed to evaluate the adsorption isotherm type as well as the influence of TiO_2: Fe_2O_3 composition on surface area and pore volume (**Figure 11**). **Figure 11(a)** displayed a

type IV isotherm, characteristic of mesoporous materials (2 - 50 nm). **Figure 11(b)** showed that increasing Fe^{2+} and Fe^{3+} concentrations as increasing Fe_2O_3 content ($TF_{0.05}$ - TF_1) enhances both surface area and pore volume, which is attributed to stronger lattice distortion, crystal defects, structural deformation, and then promotes the formation of additional pores. As pore volume increases, the surface area also rises linearly, highlighting the dominant contribution of intraparticle

porosity compared to external particle size [30]. So, at low Fe_2O_3 compositions ($TF_{0.05}$ - $TF_{0.1}$), the increase in pore volume and surface area is primarily attributed to the formation of new pores induced by the interfacial interaction between Fe_2O_3 and TiO_2. In contrast, at higher Fe_2O_3 compositions ($TF_{0.2}$ - TF_1), significant enhancement arises from Fe^{3+} incorporation into the TiO_2 lattice, which opens and enlarges internal pores.
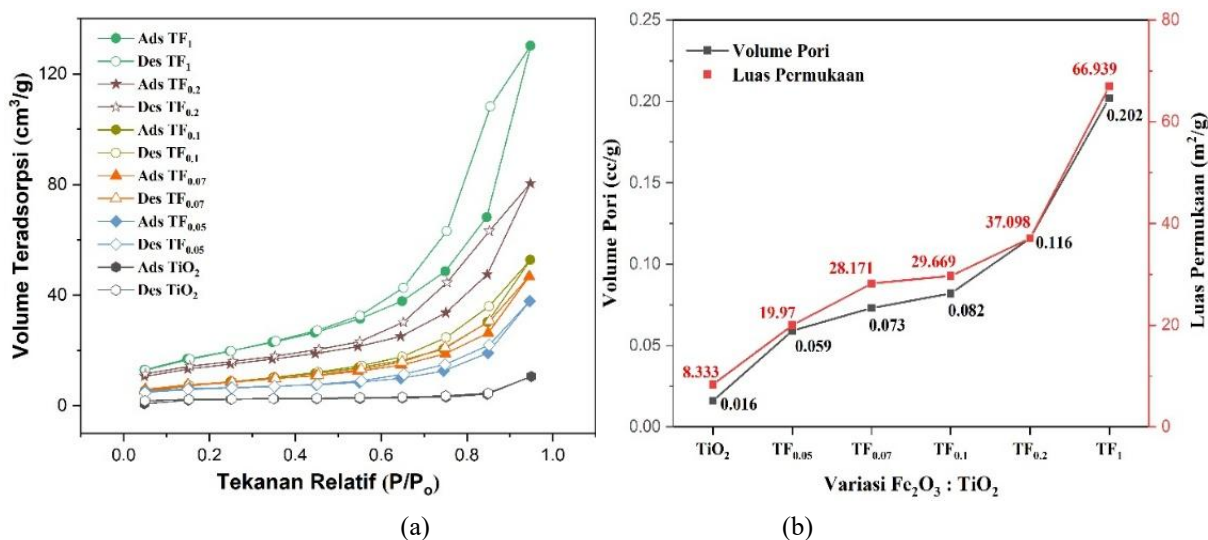

Figure 11 (a) Isotherm type and (b) Pore volume and surface area graph of composite with TiO_2: Fe_2O_3 variation.

Bandgap Analysis. The variation in the TiO_2: Fe_2O_3 ratio induces lattice distortion within TiO_2 and promotes iron oxide formation, thereby modulating both doping efficiency and interfacial interactions. These structural, optic, and electronic modifications strongly influence the bandgap of the composite, as illustrated in **Figure 12**. **Figure 12** showed that increasing concentrations of Fe^{2+} and Fe^{3+}, along with a higher Fe_2O_3/TiO_2 ratio, reduce the composite bandgap from 3.01 to 2.48 eV. This reduction is mainly attributed to the formation of heterojunctions and Fe doping,

particularly Fe^{3+}, which substitutes Ti^{4+} in the TiO_2 lattice during reaction and sintering, which introduces new electronic states within the bandgap and enhances orbital overlap between Ti 3d and Fe 3d, thus narrowing the bandgap. The doping effect is further evidenced by decreased intrinsic absorption intensity, band-tail extension toward longer wavelengths, and a redshift of the absorption edge [2,23]. Furthermore, the shift of the TiO_2 diffraction peak at $2\theta = 25.31°$ (101) toward higher angles confirms lattice contraction due to Ti^{4+} substitution by Fe^{3+} [29].
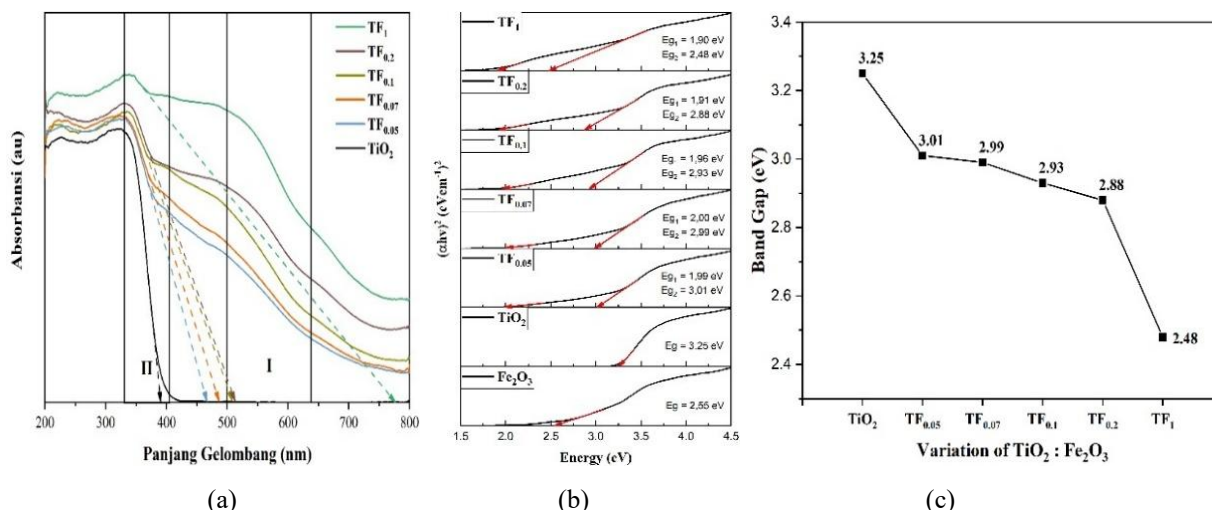
(a)   (b)   (c)

Figure 12 (a) DRS spectra, (b) tauc plots, and (c) band gap of composites with Fe_2O_3: TiO_2 compositions.

XPS Analysis. The XPS spectra of TiO_2 and its composites are shown in **Figure 13**. The composites were synthesized with TiO_2: Fe_2O_3 composition ratios of 1:0.1 ($TF_{0.1}$), 1:0.2 ($TF_{0.2}$) and 1:1 (TF_1).

(a)   (b)   (c)

(d)   (e)   (f)
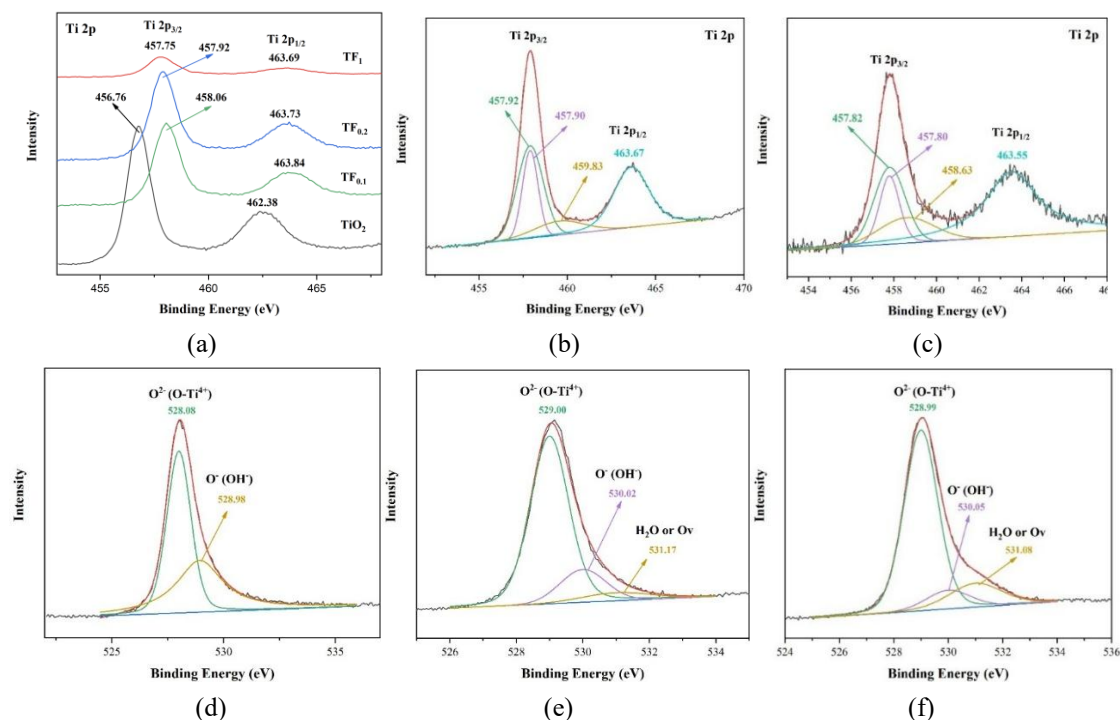
Figure 13 XPS Spectra (a) high resolution spectra (HRS) of Ti2p peak, (b) deconvolution spectra Ti2p of $TF_{0.2}$, (c) deconvolution spectra Ti2p of TF_1, (d) deconvolution spectra O1s of TiO_2, (e) deconvolution spectra O1s of $TF_{0.2}$, and (f) deconvolution spectra O1s of TF_1.

Figure 13(a) has shown a shift in the Ti 2p peak with increasing Fe_2O_3 composition. At low Fe_2O_3 content (< $TF_{0.1}$), Ti 2p peaks shift positively, indicating interfacial interaction (heterojunction) and binary oxide formation [27,31]. In contrast, at higher Fe_2O_3 loading (> $TF_{0.1}$), Ti 2p peaks shift negatively (~0.1 - 0.5 eV), signifying substitutional doping, where Fe^{3+} replaces Ti^{4+}, inducing charge imbalance, oxygen vacancies, and partial Ti^{4+} reduction to Ti^{3+}. The emergence of a new peak at 459.83 eV in deconvolution spectra (**Figures 13(b)** and **13(c)**) further confirms the presence of Ti^{3+} species [26,32]. Based on **Figures 13(d)** - **13(f)**, a new peak at 531.17 eV in the deconvoluted O 1s spectra, absent in pure TiO_2, is assigned to oxygen vacancies,

with intensity increasing from $TF_{0.1}$ to TF_1 [26]. These results demonstrate that higher Fe content enhances oxygen vacancy formation and Fe-O-Ti bonding, mainly through substitutional doping.

TEM Analysis. Simultaneously addition of Fe^{2+} and Fe^{3+} into TiO_2 powder affected the morphology and internal structure of the material as shown in **Figure 14**.

(a)   (b)   (c)
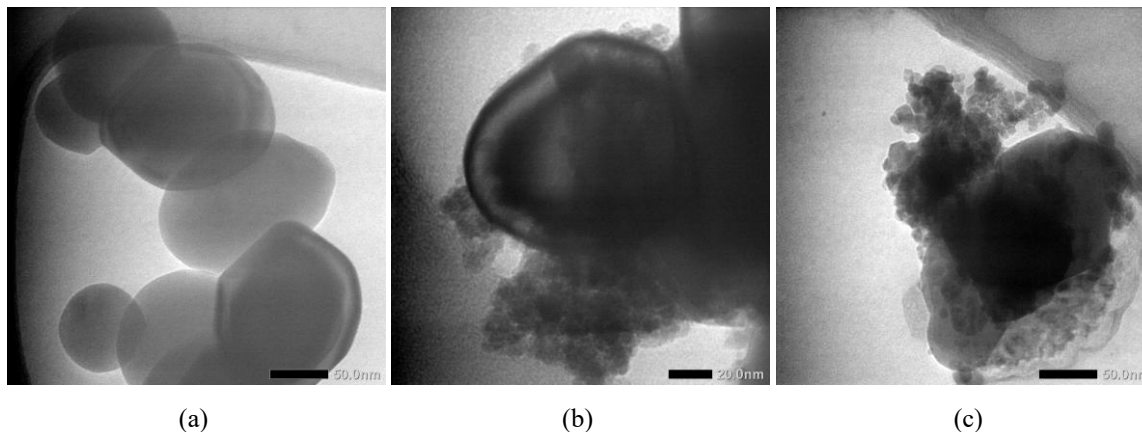
Figure 14 TEM images of (a) TiO_2 (b) $TF_{0.2}$ composite, and (c) TF_1 composite.

In the composites, Fe_2O_3 nanoparticles appear either randomly dispersed or partially forming core-shell-like aggregates within the TiO_2 matrix, confirming the presence of Fe_2O_3 phases [33]. Both TiO_2 and Fe_2O_3 tend to form agglomerates or aggregates, leading to random yet partially ordered dispersion patterns [1]. This coexistence of dispersion and aggregation indicates strong TiO_2-Fe_2O_3 interactions, which are expected to influence the photocatalytic performance of the composites.

VSM Analysis. The magnetic behavior of the composites with TiO_2: Fe_2O_3 ratio is presented in

Figure 15(a). Increasing Fe_2O_3 content enhances the magnetization moment (Ms, emu g^{-1}), mainly due to the preferential formation of maghemite (γ-Fe_2O_3) over hematite (α-Fe_2O_3), as confirmed by XRD (**Figure 9(b)**). Maghemite exhibits ferrimagnetic or paramagnetic behavior, while hematite is antiferromagnetic [34]. Increasing the magnetic properties will improve the separability and make it easier to separate the photocatalyst from the solution using an external magnet, as seen in **Figure 15(b)**.
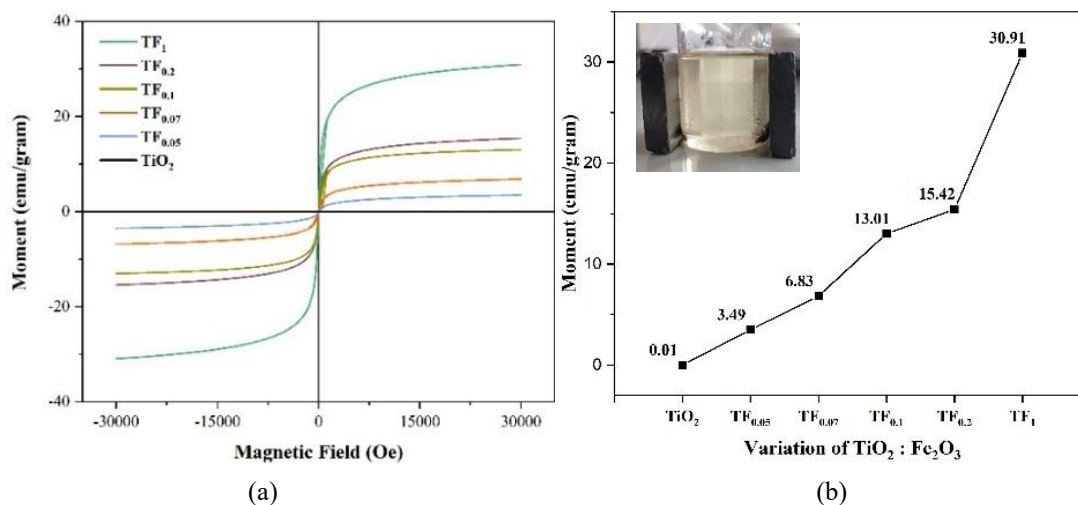

(a)   (b)

Figure 15 (a) VSM Loop hysteresis and (b) saturation magnetic (Ms) of composite with TiO_2: Fe_2O_3 composition (insert:separation with an external magnet).

Photocatalytic activity. The variation in TiO_2: Fe_2O_3 composition (mole/mole) has affected photocatalysis activities. as shown in **Figure 16**. **Figure 16** showed that increasing Fe^{2+} and Fe^{3+} concentration as increasing Fe_2O_3 composition enhances the photocatalytic activity of TiO_2 powder under visible-light irradiation. The increase in photocatalytic activity was also shown by increasing the composition of Fe^{3+} compared to Fe^{2+}. The improvement is attributed to bandgap narrowing, reduced crystallinity and crystallite size, and enlarged surface area. Based on the results, Methyl Violet (MV) degradation is more pronounced than Cr(VI) photoreduction, suggesting that Fe^{3+} primarily functions as an electron trap rather than a hole trap.
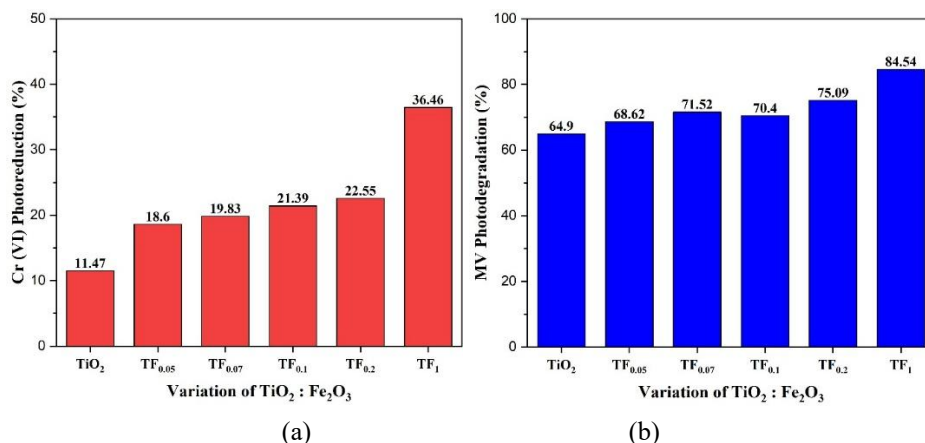

Figure 16 (a) Photoreduction of Cr(VI) and (b) MV photodegradation with TiO_2: Fe_2O_3 composition.

Correlation Analysis. Composition of Fe_2O_3 into TiO_2 powder had significantly influenced properties and photocatalysis activities, whose coefficient correlation (r) is higher than the theoretical coefficient correlation (0.959) at $\alpha = 1\%$ and $N = 5$ as shown in **Table 2**. Composition of Fe_2O_3 has negative correlation with crystal size, crystallinity, bandgap, whereas positive correlation had occurred with surface area, saturation magnetic, and photocatalytic activities of composite. Crystal size has positive correlation with crystallinity, and bandgap in nano structure, whereas negative correlation had occurred with surface area, saturation magnetic, and photocatalytic activities of composite.

Table 2 Coefficient correlation (r) between composition of Fe_2O_3 and dependent parameters.

Correlation with	Composition of Fe_2O_3	Crystal size	Crystallinity	Bandgap	Surface area	Moment magnet	Photoreduction of Cr(VI)
Composition of Fe_2O_3	1						
Crystal size	−0.9602	1					
Crystallinity	−0.9968	0.9716	1				
Bandgap	−0.9939	0.9718	0.9968	1			
Surface area	0.9765	−0.9796	−0.9905	−0.9887	1		
Moment Magnet	0.9413	−0.9603	−0.9596	−0.9722	0.9812	1	
Photoreduction of Cr(VI)	0.9955	−0.9635	−0.9979	−0.9989	0.9882	0.9669	1
Photodegradation of Methyl violet	0.9674	−0.9898	−0.9821	−0.9743	0.9920	0.9585	0.9722

Conclusions

From the preceding discussion, the conclusions were as follows:

1) Simple modification of TiO_2 powder by simultaneous addition of Fe^{2+} and Fe^{3+} ions has resulted in improved properties, enhanced visible-light response and activity although further improvements are still required.

2) Alterations in the Fe^{2+}: Fe^{3+} and TiO_2:Fe_2O_3 (TF) ratio (mole/mole) have affected composite properties with different and interesting mechanism. Overall, Fe^{3+} plays a more dominant role than Fe^{2+} in changing the properties and enhancing the photocatalytic performance of TiO_2-Fe/Fe_2O_3 composites.

3) Increasing the proportion of Fe^{3+} and Fe_2O_3 in TiO_2 powder promoted the formation of Ti-O-Fe bonds, enhanced lattice distortion and defects, reduced crystallinity, enlarged surface area, and narrowed the bandgap.

4) At lower Fe^{3+} and Fe_2O_3 contents (Fe^{2+}: Fe^{3+} = 1:0.3 - 1:1; TiO_2: Fe_2O_3 = 1:0.05 - 1:0.1 mol/mol), interfacial interaction and heterojunction formation dominate, leading to increased crystallite size. In contrast, at higher concentrations (Fe^{2+}: Fe^{3+} = 1:1 - 1:3; TiO_2: Fe_2O_3 = 1:0.2 - 1:1 mol/mol), substitutional doping predominates, resulting in reduced crystallite size.

5) The magnetic properties decreased with the greater formation of hematite as Fe^{3+} content increased but were enhanced by the growth of maghemite with higher Fe_2O_3 composition.

6) Increasing Fe^{2+} and Fe^{3+} concentration as increasing Fe_2O_3 composition enhances the photocatalytic activity of TiO_2 powder under visible-light irradiation.

Acknowledgements

Declaration of Generative AI in Scientific Writing

During the preparation of this work, the author partly used ChatGPT for paraphrasing to improve the readability and language of the manuscript. After using this tool, the author reviewed and edited the content as needed and takes full responsibility for the content of the published article.

CRediT Author Statement

Candra Purnawan: Conceptualization; Methodology; Formal analysis; Data curation; Software, Visualization; Writing - Original draft preparation. **Endang Tri Wahyuni:** Conceptualization; Supervision, Investigation; Validation. **Indriana Kartini:** Supervision, Visualization; Formal analysis. **Suherman:** Supervision, Writing - Review & Editing.

References

[1] A Kubiak, M Kubacka, E Gabała, A Dobrowolska, K Synoradzki, K Siwińska-Ciesielczyk, K Czaczyk and T Jesionowski. Hydrothermally assisted fabrication of TiO2-Fe3O4 composite materials and their antibacterial activity. *Materials* 2020; **13(21)**, 4715.

[2] VV Shymanovska, TA Khalyavka, EV Manuilov, TA Gavrilko, A Aho, VV Naumov and ND Shcherban. Effect of surface doping of TiO2 powders with Fe ions on the structural, optical and photocatalytic properties of anatase and rutile. *Journal of Physics and Chemistry of Solids* 2022; **160**, 110308.

[3] N Madima, KK Kefeni, SB Mishra, AK Mishra and AT Kuvarega. Fabrication of magnetic recoverable Fe3O4/TiO2 heterostructure for photocatalytic degradation of Rhodamine B dye. *Inorganic Chemistry Communications* 2022; **145**, 109966.

[4] E Savitri, SW Yunita, C Winoto and RK Widi. Innovative waste benzene remediation by enhanced photocatalytic with TiO2/Fe3O4-Based material supported by bentonite in batch and continuous system. *Trends in Sciences* 2024; **21(7)**, 7872.

[5] C Afonso, O Lima, IR Segundo, S Landi, E Margalho, N Homem, M Pereira, MFM Costa, E Freitas and J Carneiro. Effect of Iron-doping on

the structure and photocatalytic activity of TiO2 nanoparticles. *Catalysts* 2023; **13(1)**, 58.

[6] P Sun, S Han, J Liu, J Zhang, S Yang, F Wang, W Liu, S Yin, Z Ning and W Cao. Introducing oxygen vacancies in TiO2 lattice through trivalent iron to enhance the photocatalytic removal of indoor NO. *International Journal of Minerals, Metallurgy and Materials* 2023; **30**, 2025-2035.

[7] B Taudul, F Tielens and M Calatayud. On the origin of raman activity in anatase TiO2 (Nano) materials: An *Ab initio* investigation of surface and size effects. *Nanomaterials* 2023; **13(12)**, 1856.

[8] SJ Babu, VN Rao, DHK Murthy, MMM Shastri, M Shetty, KSA Raju, PD Shivaramu, CSA Kumar, MV Shankar and D Rangappa. Significantly enhanced cocatalyst-free H_2 evolution from defect-engineered Brown TiO2. *Ceramics International* 2021; **47(10)**, 14821-14828.

[9] AHA Gonçalves, PHC Siciliano, OC Alves, DV Cesar, CA Henriques and AB Gaspar. Synthesis of a magnetic Fe3O4/RGO composite for the rapid photo-fenton discoloration of indigo carmine dye. *Topics in Catalysis* 2020; **63**, 1017-1029.

[10] CV Tran, PTH Nguyen, DD Nguyen, HTT Pham, DT Do and DD La. Facile fabrication of Fe2O3/TiO2 composite from titanium slag as adsorbent for As(V) removal from aqueous media. *Sustainability* 2023; **15(9)**, 7253.

[11] TT Loan, VH Huong, NT Huyen, LV Quyet, NA Bang and NN Long. Anatase to rutile phase transformation of iron-doped titanium dioxide nanoparticles: The role of iron content. *Optical Materials* 2021; **111**, 110651.

[12] MD Patekari, KK Pawar, GB Salunkhe, PM Kodam, MN Padvi, PP Waifalkar, KK Sharma and PS Patil. Synthesis of maghemite nanoparticles for highly sensitive and selective NO_2 sensing. *Materials Science and Engineering: B* 2021; **272**, 115339.

[13] N Abbas, GN Shao, MS Haider, SM Imran, SS Park and HT Kim. Sol-gel synthesis of TiO2-Fe2O3 systems: Effects of Fe2O3 content and their photocatalytic properties. *Journal of Industrial and Engineering Chemistry* 2016; **39**, 112-120.

[14] ES Wibowo and B-D Park. Determination of crystallinity of thermosetting urea-formaldehyde resins using deconvolution method. *Macromolecular Research* 2020; **28**, 615-624.

[15] MS Khan, JA Shah, N Riaz, TA Butt, AJ Khan, W Khalifa, HH Gasmi, ER Latifee, M Arshad, AAA Al-Naghi, A Ul-Hamid, M Arshad and M Bilal. Synthesis and characterization of Fe-TiO2 nanomaterial: Performance evaluation for RB5 decolorization and *in vitro* antibacterial studies. *Nanomaterials* 2021; **11(2)**, 436.

[16] AM Oviedo, H Truong Thi, QC Van and HH Nguyen. Physicochemical properties of Fe-doped TiO2 and the application in Dye-sensitized solar cells. *Optical Materials* 2023; **137**, 113587.

[17] R Hatefi, H Younesi, A Mashinchian-Moradi and S Nojavan. A facile decoration of anatase Fe3O4/TiO2 nanocomposite with graphene quantum dots: Synthesis, characterization, and photocatalytic activity. *Advanced Powder Technology* 2021; **32(7)**, 2410-2422.

[18] S Pan, M Zha, C Gao, J Qu and X Ding. Pore structure and fractal characteristics of organic-rich lacustrine shales of the kongdian formation, cangdong sag, bohai bay basin. *Frontiers in Earth Science* 2021; **9**, 760583.

[19] FJ Sotomayor, KA Cychosz and M Thommes. Characterization of micro/mesoporous materials by physisorption: Concepts and case studies. *Accounts of Materials & Surface Research* 2018; **3(2)**, 34-50.

[20] S Badawy and P Pandey. Chapter 28 - design, development, and scale-up of the high-shear wet granulation process. *Developing Solid Oral Dosage Forms (Second Edition)* 2017; **2017**, 749-776.

[21] YQ Cao, TQ Zi, XR Zhao, C Liu, Q Ren, JB Fang, WM Li and AD Li. Enhanced visible light photocatalytic activity of Fe2O3 modified TiO2 prepared by atomic layer deposition. *Scientific Reports* 2020; **10**, 13437.

[22] A Khalid, P Ahmad, AI Alharth, S Muhammad, MU Khandaker, MRI Faruque, IU Din and MA Alotaibi. A practical method for incorporation of Fe (III) in Titania matrix for photocatalytic applications. *Materials Research Express* 2021; **8(4)**, 045006.

[23] M Gao, L Zhu, CK Peh and GW Ho. Solar absorber material and system designs for photothermal water vaporization towards clean water and energy production. *Energy and Environmental Science* 2019; **12(3)**, 841-864.

[24] E Inico, C Saetta and GD Liberto. Impact of quantum size effects to the band gap of catalytic materials: A computational perspective. *Journal of Physics Condensed Matter* 2024; **36(36)**, 361501.

[25] P Kaur and G Verma. Converting fruit waste into carbon dots for bioimaging applications. *Materials Today Sustainability* 2022; **18**, 100137.

[26] C Wen, X Ni, M Han, Y Yu, C Liu, Y Zhang, B Zheng and S Feng. The function of photocatalytic performance and carrier separation efficiency tuned by doping content in homogeneous photocatalysts. *Advanced Science* 2025; **12(25)**, 2501026.

[27] N Kanjana, W Maiaugree, P Poolcharuansin and P Laokul. Synthesis and characterization of Fe-doped TiO_2 hollow spheres for dye-sensitized solar cell applications. *Materials Science and Engineering: B* 2021; **271**, 115311.

[28] M Coduri, P Masala, L Bianco, F Spizzo, D Ceresoli, C Castellano, S Cappelli, C Oliva, S Checchia, M Allieta, DV Szabo, S Schlabach, M Hagelstein, C Ferrero and M. Scavini. Local structure and magnetism of Fe2O3 maghemite nanocrystals: The role of crystal dimension. *Nanomaterials* 2020; **10(5)**, 867.

[29] AA Isari, A Payan, M Fattahi, S Jorfi and B Kakavandi. Photocatalytic degradation of rhodamine B and real textile wastewater using Fe-doped TiO_2 anchored on reduced graphene oxide (Fe-TiO2/rGO): Characterization and feasibility, mechanism and pathway studies. *Applied Surface Science* 2018; **462**, 549-564.

[30] MSM Zaini and SSA Syed-Hassan. Effects of different physical activation agents on adsorbent pore development and methane uptake. *Recent Innovations in Chemical Engineering* 2022; **15(2)**, 127-137.

[31] A Srivastava, JAK Satrughna, MK Tiwari, A Kanwade, SC Yadav, K Bala and PM Shirage. Effect of Ti1-xFexO2 photoanodes on the performance of dye-sensitized solar cells utilizing natural betalain pigments extracted from *Beta vulgaris (BV)*. *Energy Advances* 2023; **2(1)**, 148-160.

[32] E Faustino, TF da Silva, RF Cunha, DRV Guelfi, PS Cavalheri, SC de Oliveira, ARL Caires, GA Casagrande, RP Cavalcante and AM Junior. Synthesis and characterization of N and Fe-Doped TiO_2 nanoparticles for 2,4-Dimethylaniline mineralization. *Nanomaterials* 2022; **12(15)**, 2538.

[33] VE Novala and JG Carriazo. Fe_3O_4-TiO_2 and Fe_3O_4-SiO_2 core-shell powders synthesized from industrially processed magnetite (Fe_3O_4) microparticles. *Materials Research* 2019; **22(3)**, 20180660.

[34] PRS Baabu, HK Kumar, MB Gumpu, J Babu K, AJ Kulandaisamy and JBB Rayappan. Iron oxide nanoparticles: A review on the province of its compounds, properties and biological applications. *Materials* 2023; **16(1)**, 59.